In-situ XPS investigation of the SEI formed on LGPS and LAGP with metallic lithium
SUPPLEMENTARY INFORMATION

Yi Liang[1], Matthew Burton[1,2], Ben Jagger[1], Hua Guo[1,2], Johannes Ihli[1], and Mauro Pasta[1,2]

[1]Department of Materials, University of Oxford, Parks Road, Oxford OX1 3PH, United Kingdom
[2]The Faraday Institution, Quad One, Becquerel Avenue, Harwell Campus, Didcot OX11 0RA, United Kingdom

Experimental

Materials

Solid electrolyte $Li_{1.5}Al_{0.5}Ge_{1.5}(PO_4)_3$ (99.99% pure, D50=500 nm) was purchased from Ampcera^{TM} through MSE Supplies LLC. Li ribbon (99.9% pure) was purchased from Sigma-Aldrich. The $Li_{10}GeP_2S_{12}$ SE was synthesised through a ball milling and heat treatment method. The precursors Li_2S (99.98%, Merck), GeS_2 (MP Biomedicals), and P_2S_5 (99%, Merck), in the stoichiometric ratio, along with an additional 2 wt% sulphur (sublimed, Alfa Aesar), were mechanically milled at 700 rpm for 5 hours in sealed ball-milling jars. The resulting mixture was pelletised and annealed at 550 °C for 8 hours in an argon-filled glovebox. After naturally cooling to room temperature, the pellet was ground, and the final product, $Li_{10}GeP_2S_{12}$ powder (as shown by XRD in Figure S12), was collected.

XPS sample preparation

LAGP pellets were prepared through the following procedure. Initially, 150 mg of LAGP powder was cold-pressed under 150 MPa using a 10 mm die press. The pressed pellets underwent a high-temperature sintering process in a box furnace at 900°C for 10 hours in an air environment. The furnace temperature ramping rate was set at 2°C min^{-1}, and to compensate for Li loss, the pellet was placed on top of a LAGP powder bed. Subsequently, the sintered pellets were polished using sandpaper with grit ranging from 800 to 4000, resulting in a smooth surface on both sides. The size of the sintered pellets was about 850 µm in thickness and 8.38 mm in diameter. LGPS pellets were prepared by cold pressing 150 mg powder at 400 MPa using a 8 mm die.

For the virtual plating sample, the SE pellet was pressed on top of a pre-punched 8 mm Li disk, which was affixed to a thin copper disk at a much lower pressure of 40 MPa. Then the sample stack was stuck onto the XPS stage using carbon tape with the Li-foil-free surface facing up and transferred to the XPS intro chamber from the glovebox using an air-tight transfer vessel. The Li metal used in this experiment was firstly brushed using a toothbrush to eliminate surface contamination and subsequently calendered to achieve a smooth surface. The pressed pellet was stuck onto the sample stage without any further treatments for the *in-situ* sputtering experiment.

VEP-XPS experimental setup

XPS experiments were conducted using the PHI VersaProbe III with an Al Kα X-ray (hν=1486.6 eV) source. The pressure inside the XPS chamber was at 10^{-7} Pa level. During the VEP-XPS experiment, the XPS instrument integrated electron neutraliser gun, acting as a virtual electrode, was used to provide a constant flux of electrons to the SE pellets surface; driving Li^+ migration upwards through the SE. The combination of migrated Li^+ and neutraliser-provided electrons at the top surface of the SE results in the gradual formation of metallic Li species.

The measurement point was located at the centre of the pellet using X-ray-induced secondary electron images (SXI), and the electron beam was also focused on the pellet centre. The applied beam current was 20 µA for both LGPS and LAGP SEs, corresponding to 0.0398 mA/cm^2 and 0.0361 mA/cm^2 in current density respectively. The plating rate was calculated based on passed charge, which is ∼3.24 nm/min for LGPS SE, and ∼2.94 nm/min for LAGP SE. The electron beam plating and XPS acquisition were performed alternatively to study the SEI evolution. For the *in-situ* sputtering experiment, the ion gun beam voltage was set as 4 kV and the Li metal target was directly facing the Ar^+ ion gun during the sputtering process. The sputtering rate was estimated as 0.14 nm/min reported by Narayanan *et al.* using the same experiment setup.[1] The Li metal sputtering and XPS measurements were conducted alternatively to probe the evolution of the surface chemistry information.

The XPS probing area was 500 µm × 500 µm, and all measurements were performed with the neutraliser off. The pass energy for the survey scan was 224 eV and 55 eV for the high-resolution scan. Collected spectra were processed using CasaXPS software and were calibrated based on C 1s to 248.8 eV (unless specified).[2]

Supplementary Figures

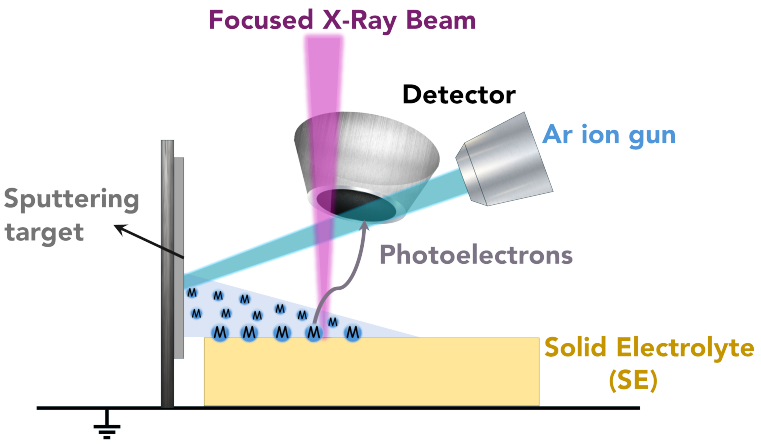

Figure S1: Schematic of the *in-situ* sputtering experimental setup: Fresh Li metal is adhered to the target wall, and the Ar^+ gun is employed to sputter the Li onto the SE surface. Subsequently, the Li sputtering and XPS acquisition are conducted alternately to probe the SEI evolution.

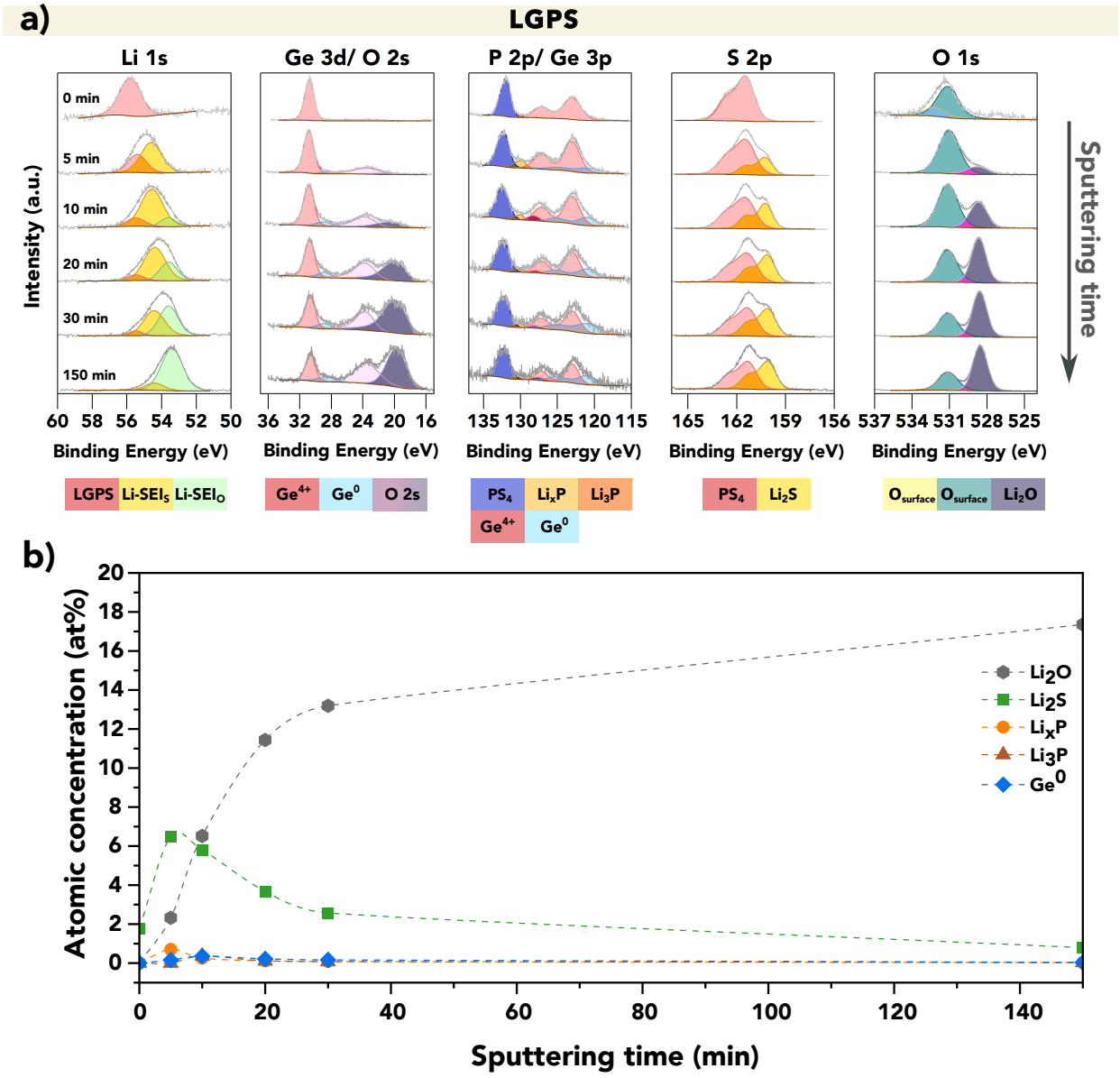

Figure S2: XPS core spectra evolution of *in-situ* sputtering experiments of LGPS SE **(a)**, with sputtering time and decomposition products labelled, ps: the peak intensity is normalised to show the deconvoluted results; **(b)** The atomic concentration variation with sputtering time.

Here, the XPS spectrum taken after 150 minutes of sputtering, shown in Figure S2a, doesn't exhibit a detectable metallic Li peak. This absence indicates rapid reaction kinetics between LGPS and LMA, and the formation of a non-passivating SEI layer.

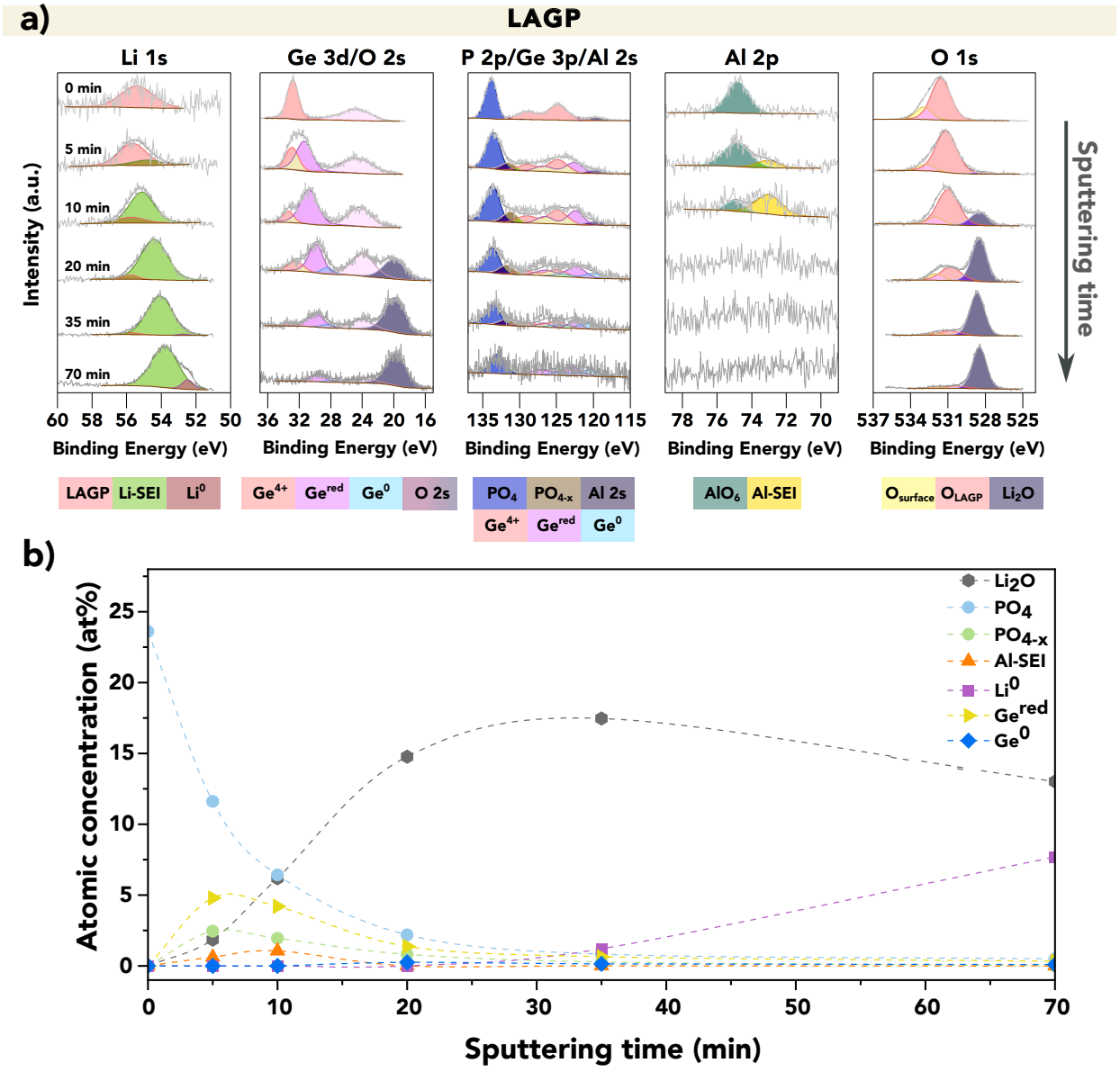

Figure S3: XPS core spectra evolution of *in-situ* sputtering experiments of LAGP SE **(a)**, with sputtering time and decomposition products labelled, ps: the peak intensity is normalised to show the deconvoluted results; **(b)** The atomic concentration variation with sputtering time. Charge calibration is carried out based on P 2p peak for PO_4.

As evidenced by the Li^0 peak in Figure S3a Li 1s spectra, the SEI formation kinetics between the LAGP and LMA shows a reduced rate compared to the LGPS SE. Unlike what has been observed in the VEP-XPS experiment, the degradation process of the LAGP SE follows a less direct route. One contributing factor could be the rapid formation of Li_2O when Li was sputtered on top of the SE. The formed Li_2O, act as an insulating layer, effectively mitigating the reaction between LAGP and the Li metal. The Ge^{4+} undergoes initial reduction to the intermediate state Ge^{red} before reaching the metallic state.

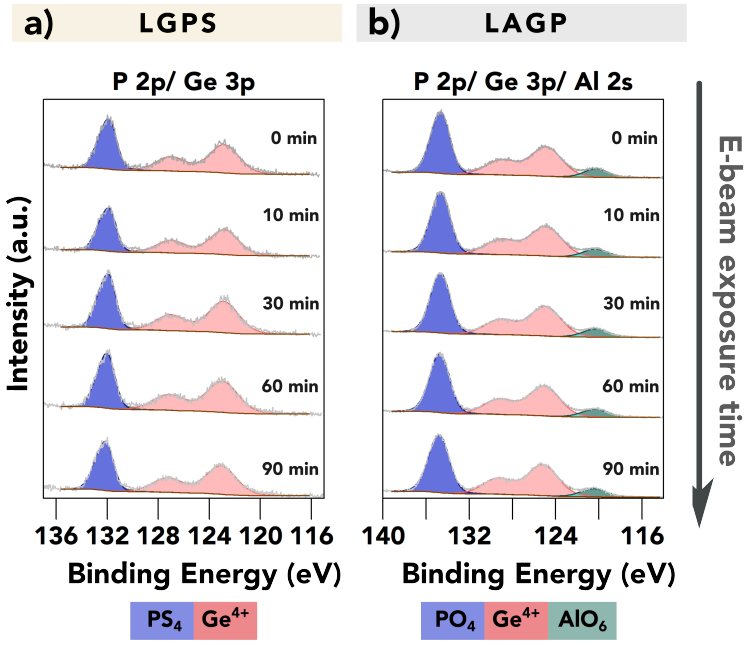

Figure S4: XPS spectra for VEP-XPS experiment of LGPS **(a)** and LAGP **(b)** SE without Li source underneath the pellet, the e$^-$-beam exposure time is labelled in both panels, ps: the peak intensity is normalised to show the deconvoluted results.

Here, the LAGP pellet, approximately 8.4 mm in diameter, was exposed to a 20 µA electron beam. LGPS was cold-pressed into a 5 mm pellet, and the current for the electron neutraliser was adjusted to 10 µA to accommodate the smaller pellet size. In both cases, no discernible change was observed with increasing e$^-$-beam exposure time. This confirms that the observed BE shift during the VEP-XPS experiments, with the Li source underneath, is caused by the reaction with plated Li rather than the e$^-$-beam.

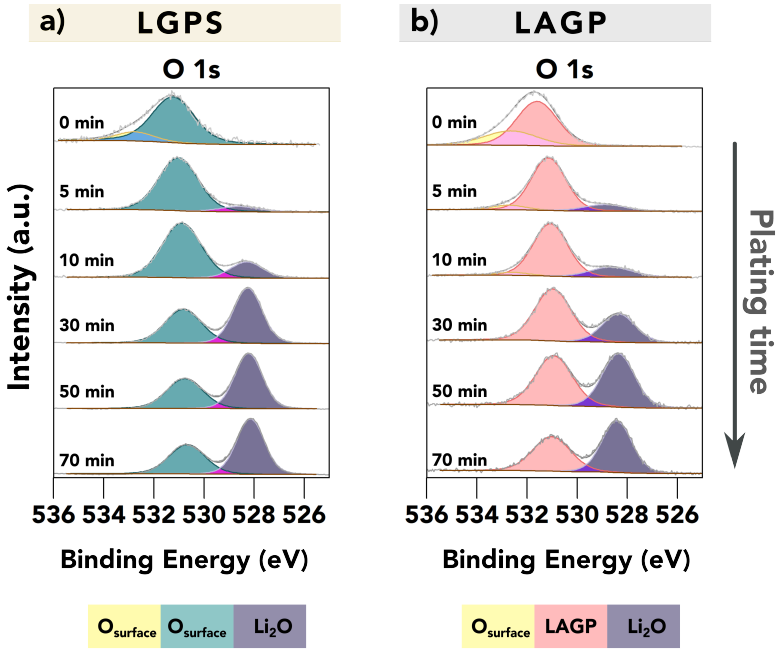

Figure S5: The plots show time series of O 1s core-level spectra acquired during VEP-XPS experiments on top of **(a)** LGPS and **(b)** LAGP. The total Li plating time (e^--beam exposure time) is given in both panels. Acquired spectra (grey) are shown along with linear combination fitting results. The individual spectral components are coloured; a key is provided below each group of spectra, ps: the peak intensity is normalised.

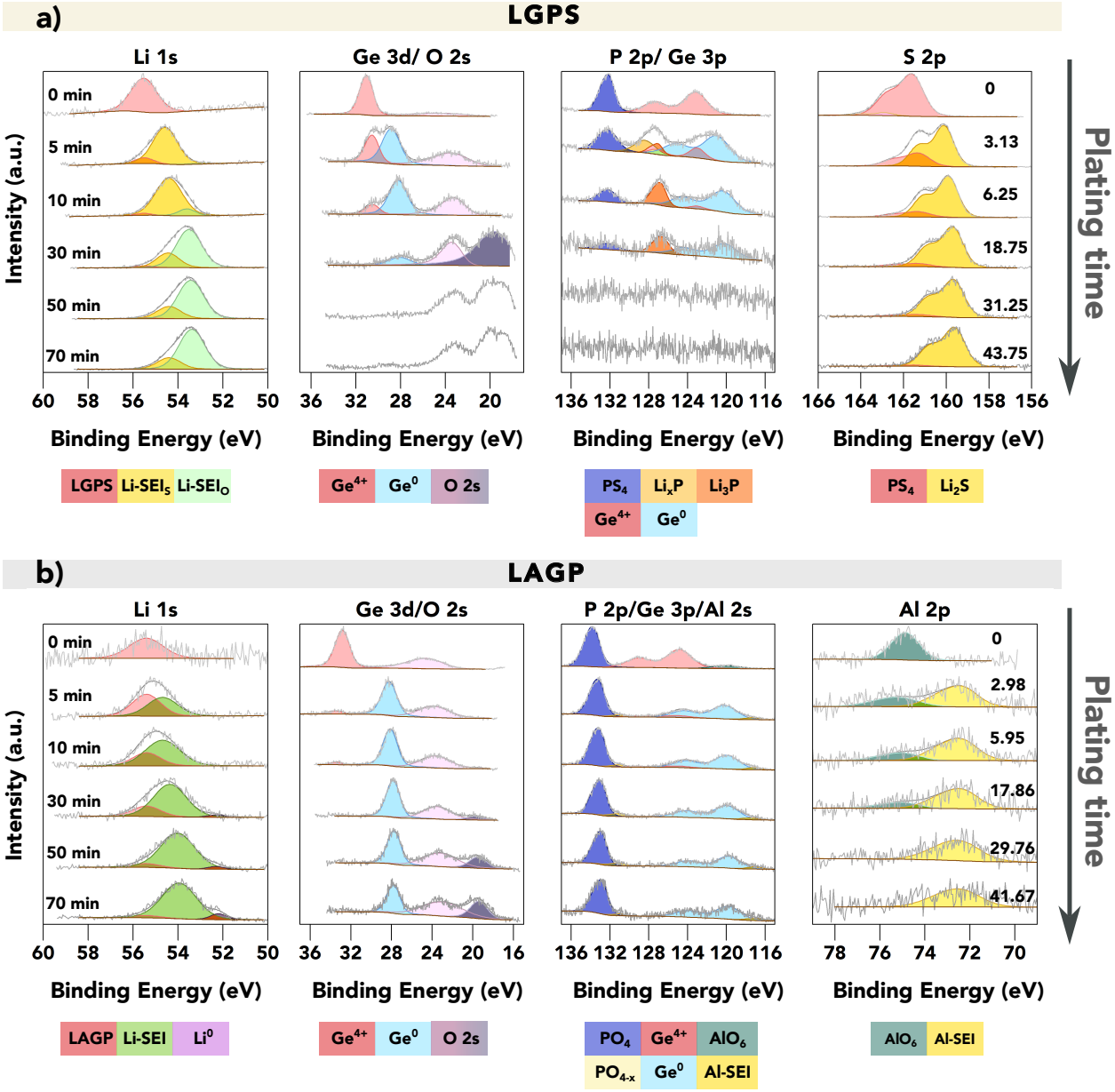

Figure S6: VEP-XPS investigations of LGPS and LAGP. The plots show time series of XPS core spectra acquired during VEP-XPS experiments examining the SEI formation on top of **(a)** LGPS and **(b)** LAGP. The total Li plating time (e^--beam exposure time) is given in the first column, and the passed charge q_A ($\mu Ah \cdot cm^{-2}$), normalised by area, is labelled in the last column. Acquired spectra (grey) are shown along with linear combination fitting results. The individual spectral components are coloured; a key is provided below each group of spectra. For LGPS SE, two Li 1s SEI peaks are labelled in two colours with the subscripts donating the main non-Li contributing element, as their close BE values make it difficult to deconvolute the peaks accurately. The peak intensities were normalised for each acquired core spectrum to improve the visibility of minor spectral contributions. The applied beam current was 20 µA for both samples. This is a zoom in version of Figure 2.

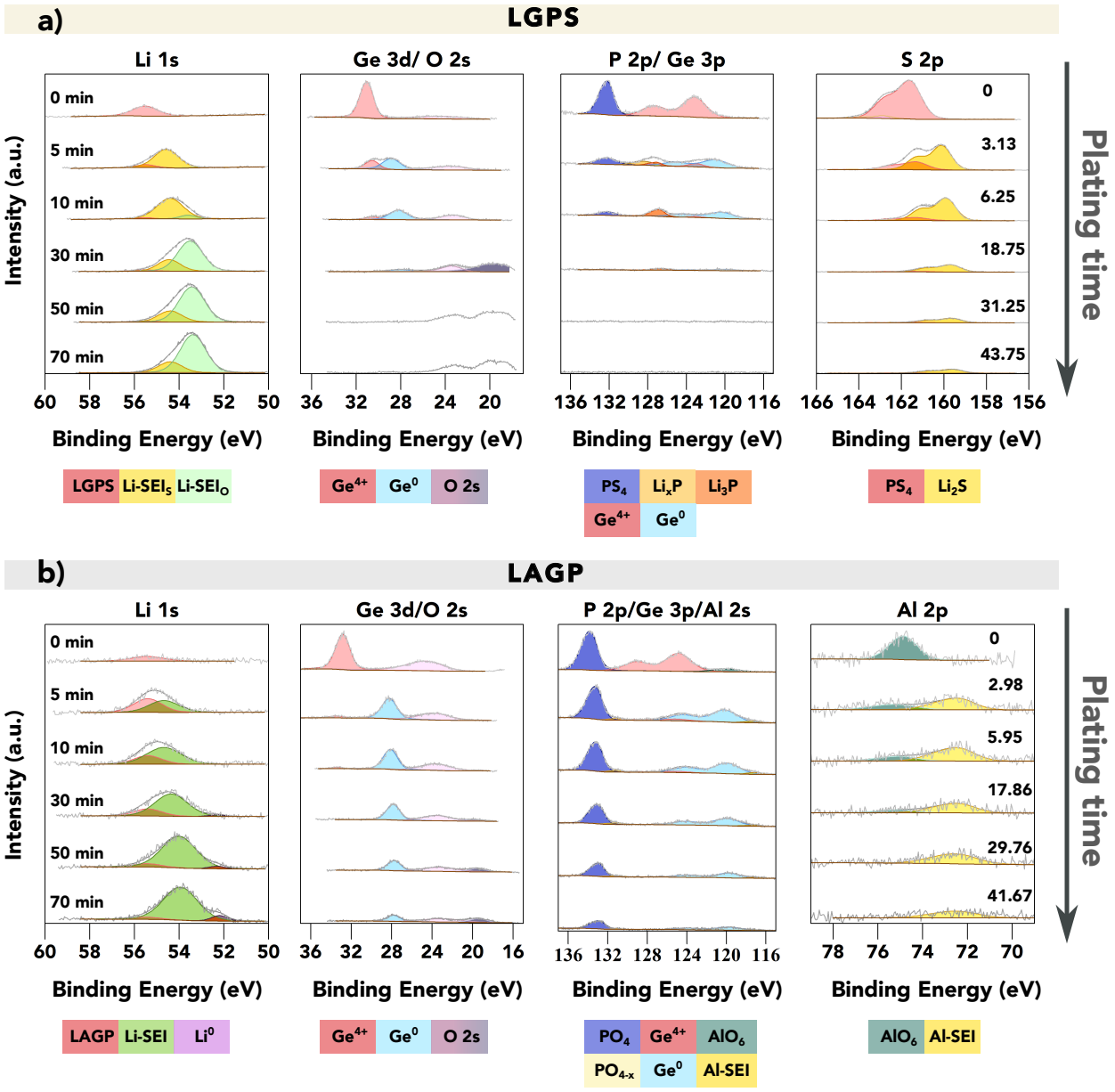

Figure S7: VEP-XPS Investigations of LGPS and LAGP. Shown is a time series of XPS core spectra acquired during virtual Li plating XPS experiments examining the SEI formed on top of **(a)** LGPS and **(b)** LAGP. The total Li plating time (e^--beam exposure time) is given in the first column. Shown are the acquired spectra (grey) and linear combination fitting results. The individual components/assigned species are coloured with labels provided below the spectra. The peak intensities were not normalised for each acquired core spectra (non-normalised version of Figure 2), to ease the visibility of signal intensity evolution of minor spectra contributions. The applied beam current was 20 µA for both samples.

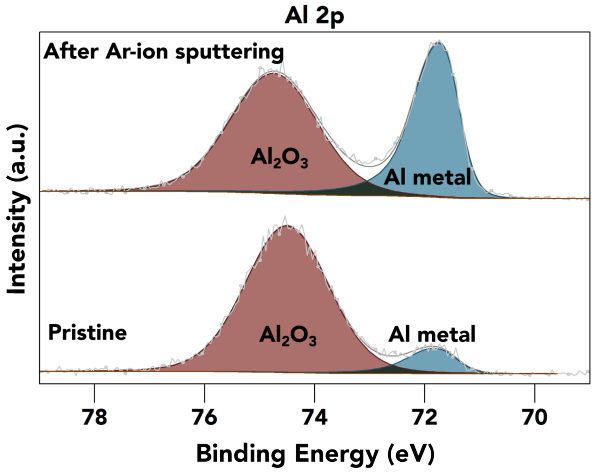

Figure S8: XPS measurement of aluminium foil.

Shown in Figure S8 is the XPS measurement of aluminium foil used as a reference to validate the chemical state of Al element in the SEI. Here, Al^{3+} in aluminium oxide has a BE of 74.4 eV, and the metallic Al has a BE of 71.6 eV. The secondary Al-SEI labelled in the Al 2p core-level spectra has a BE of 72.3 eV, which is approximately 0.7 eV away from the BE position of metallic Al, suggesting the Al-SEI is not in its metallic form.

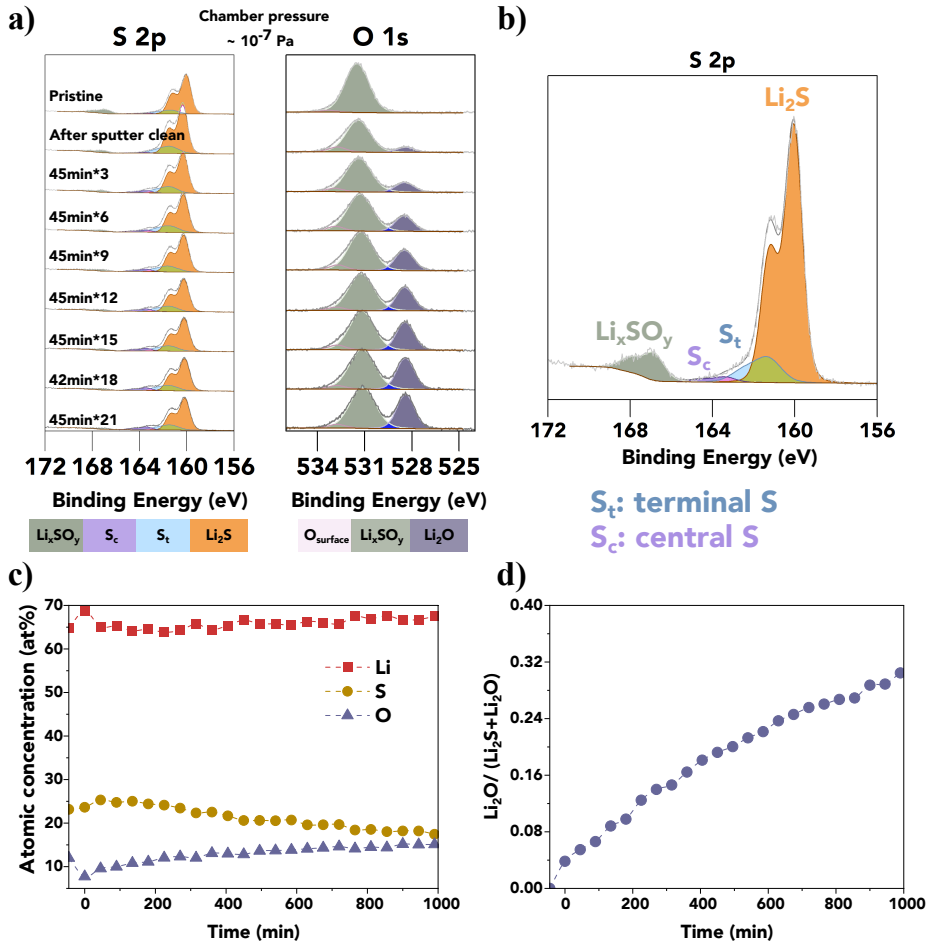

Figure S9: XPS measurement of Li_2S sample inside the XPS chamber over time: **(a)** S 2p and O 1s core-level spectra. In the sequence of XPS spectra presented here, the progression from top to bottom reflects the information of the pristine surface, followed by the surface after gentle Ar-ion sputter cleaning, and subsequently, the changes observed on the sample surface over time. Each sequence of XPS measurement was conducted over a duration of 45 minutes (labelled in the first column); **(b)** Enlarged XPS S 2p spectrum of the pristine surface showing detailed fitting results; **(c)** The evolution of Li, S and O atomic concentration over time; **(d)** Evolution of the ratio of Li_2S/ (Li_2S+Li_2O).

The pristine Li_2S powder (99.98% trace metal basis) was purchased from Sigma-Aldrich and then pelletized under 500 MPa. Figure S9b is the deconvoluted result for the S 2p core-level spectrum, which indicated the existence of polysulfide and oxidation product in the purchased powder. The pelletized Li_2S sample was subjected to continuous XPS measurement inside the XPS chamber with the neutraliser on to track its changes over time. The results indicated a progressive formation of Li_2O on the surface, as evidenced by the increasing intensity of Li_2O peak as labelled in S9a. Figure S9c and d show the increasing atomic concentration of oxygen and the ratio of Li_2O over the sum of (Li_2S and Li_2O) respectively. These trends suggest that the Li_2S reacts with the residual contaminants present inside the XPS chamber, resulting in the formation of Li_2O during XPS measurements. This observation explains the reason for the continuous formation of Li_2O on the surface of LGPS SE during the *in-situ* XPS experiment, as its SEI contains a large fraction of Li_2S. By extension, it also explains the formation of Li_2O on the surface of other sulphide SE that inherently lack oxygen in their composition during *in-situ* XPS experiments before the detection of Li^0 peak, for example, the argyrodite Li_6PS_5Cl.[1]

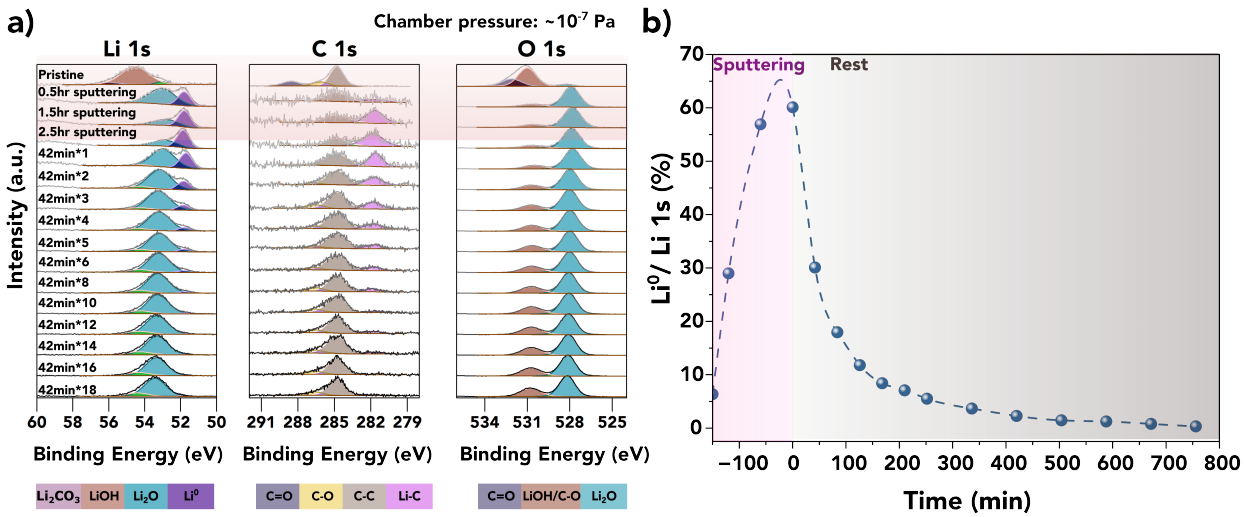

Figure S10: XPS measurement of Li metal sample inside the XPS chamber over time: **(a)** Li 1s, C 1s and O 1s core-level spectra. In the sequence of XPS spectra presented here, the progression from top to bottom reflects the information of the pristine surface, followed by the surface after Ar-ion sputter cleaning, and subsequently, the changes observed on the sample surface over time. Each sequence of XPS measurement was conducted over a duration of 42 minutes (labelled in the first column);**(b)** Evolution of the compositional fraction of Li^0/ Li 1s.

The lithium foil prepared for the XPS measurement was brushed and scraped to remove the surface contamination before being transferred to the XPS chamber. However, the XPS data shown in Figure S10a labelled with pristine at the top suggests the existence of a surface passivation layer as evidenced by the absence of the Li^0 peak. Then the Ar-ion sputtering was conducted to remove the passivation layer and expose the fresh metallic surface. The formation of lithium carbide was observed after the Ar-ion sputtering, likely resulting from the reaction that happens to lithium carbonates and other contaminants during the Ar-ion sputtering process.[3] Then, XPS measurements on the sputter-clean surface were conducted continuously without further treatment to evaluate the oxidation rate inside the XPS chamber. As depicted in Figure S10a , the freshly exposed lithium surface went through a continuous oxidation reaction evidenced by the increasing peak intensity of Li_2O. Figure S10b tracks the evolution of the compositional fraction of metallic lithium Li^0 over time within the Li 1s spectra, illustrating a declining fraction of Li^0. After approximately 400 minutes of measurement, a relatively thick oxide layer had formed on the surface with the fraction of Li^0 approaching zero. This progression underscores the dynamic changes in the chemical state of metallic lithium during the XPS measurement under the UHV environment inside the chamber, providing insights into the stability of metallic lithium under the XPS experimental condition.

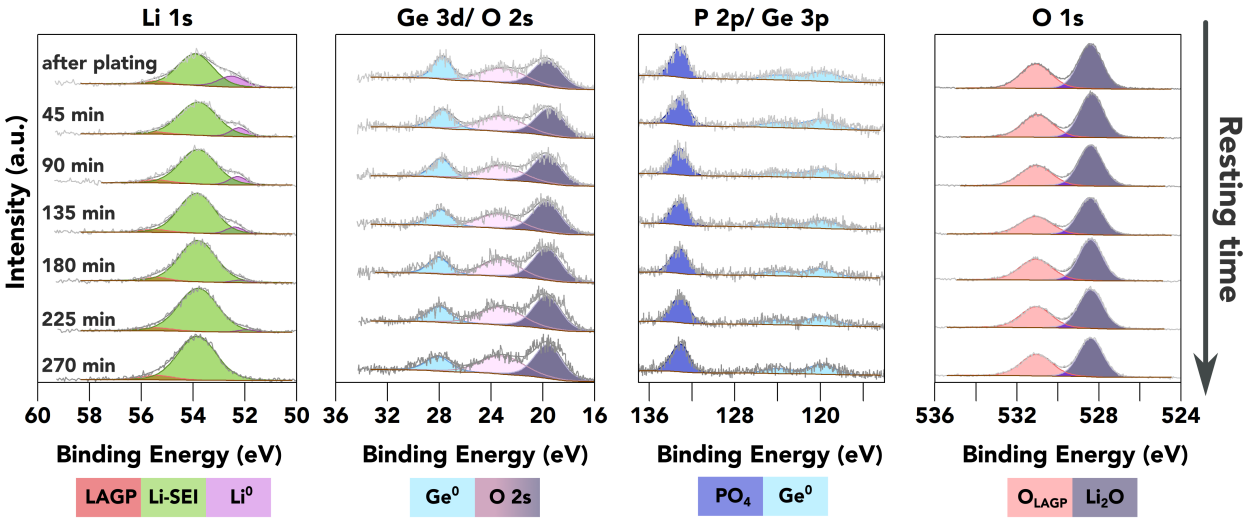

Figure S11: XPS investigation of the further reaction of plated Li metal with the underneath layer. The plots show a time series of XPS core spectra acquired after a strong Li^0 peak was observed on top of LAGP. The resting time is given in the first column. This is a zoom in version of Figure 4.

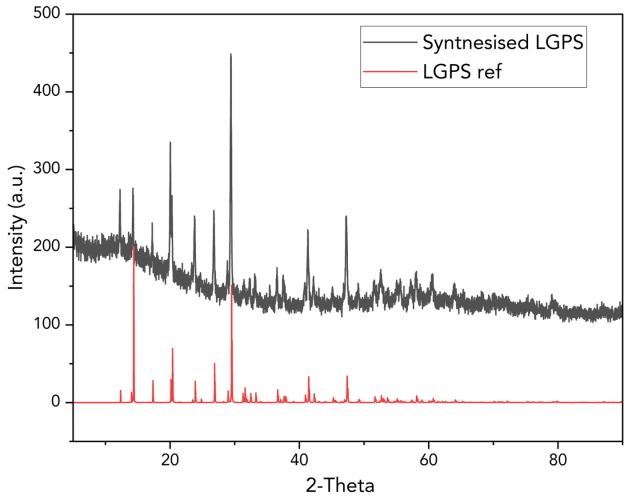

Figure S12: XRD spectra of the synthesised LGPS powder with ref spectra[4] shown in red colour.

Table S1: Electrical and ionic conductivities of different SEI components

Component	Electronic conductivity (S/cm) at 298K	Ionic conductivity (S/cm) at 298K
Li_2O[5]	10^{-14}	10^{-12}
$AlPO_4$[6–10]	10^{-8}	low
$LiAlO_2$[11,12]	insulating	10^{-9}
Li_3PO_4[13,14]	10^{-9}	10^{-8}
$Li_4P_2O_7$[15]	10^{-9}(80 °C)	insulating
Li_2S[16,17]	10^{-9}	10^{-8}
Li_3P[18,19]	10^{-4}	10^{-4}
Ge[20,21]	10^{-2}	10^{-2}

References

(1) Narayanan, S.; Ulissi, U.; Gibson, J. S.; Chart, Y. A.; Weatherup, R. S.; Pasta, M. *Nature Communications* **2022**, *13*, 7237.

(2) Fairley, N.; Fernandez, V.; Richard-Plouet, M.; Guillot-Deudon, C.; Walton, J.; Smith, E.; Flahaut, D.; Greiner, M.; Biesinger, M.; Tougaard, S.; Morgan, D.; Baltrusaitis, J. *Applied Surface Science Advances* **2021**, *5*, 100112.

(3) She, F.; Gao, A.; Jiang, P.; Zhou, Y.; Zhang, X.; Yang, M.; Gong, L.; Chen, J.; Lu, X.; Xie, F. *Vacuum* **2023**, *211*, 111893.

(4) Kuhn, A.; Köhler, J.; Lotsch, B. V. *Physical Chemistry Chemical Physics* **2013**, *15*, 11620–11622.

(5) Lorger, S.; Usiskin, R.; Maier, J. *Journal of The Electrochemical Society* **2019**, *166*, A2215–A2220.

(6) Youssif, M.; Mohamed, F.; Aziz, M. *Materials Chemistry and Physics* **2004**, *83*, 250–254.

(7) Campanella, D.; Krachkovskiy, S.; Faure, C.; Zhu, W.; Feng, Z.; Savoie, S.; Girard, G.; Demers, H.; Vijh, A.; George, C.; Armand, M.; Belanger, D.; Paolella, A. *ChemElectroChem* **2022**, *9*.

(8) Mariappan, C. R.; Yada, C.; Rosciano, F.; Roling, B. *Journal of Power Sources* **2011**, *196*, 6456–6464.

(9) Kotobuki, M.; Koishi, M. *Ceramics International* **2013**, *39*, 4645–4649.

(10) KHALIL, M. S.; HANNA, A. A.; EL-SAYED, M. A. *Phosphorus Research Bulletin* **2002**, *14*, 77–87.

(11) Indris, S.; Heitjans, P.; Uecker, R.; Roling, B. *Journal of Physical Chemistry C* **2012**, *116*, 14243–14247.

(12) Wohlmuth, D.; Epp, V.; Bottke, P.; Hanzu, I.; Bitschnau, B.; Letofsky-Papst, I.; Kriechbaum, M.; Amenitsch, H.; Hofer, F.; Wilkening, M. *Journal of Materials Chemistry A* **2014**, *2*, 20295–20306.

(13) Jodi, H.; Supardi, S.; Kartini, E.; Zulfia, A. *Jurnal Sains Materi Indonesia* **2018**, *18*, 1.

(14) BATES, J. *Solid State Ionics* **1992**, *53-56*, 647–654.

(15) El-Shinawi, H.; Cussen, E. J.; Cussen, S. A. *Dalton Transactions* **2024**, *53*, 4139–4146.

(16) Choi, S.; Yoon, I.; Nichols, W. T.; Shin, D. *Ceramics International* **2018**, *44*, 7450–7453.

(17) Hakari, T.; Hayashi, A.; Tatsumisago, M. *Chem. Lett* **2015**, *44*, 1664–1666.

(18) Li, J.; Liu, D.; Sun, H.; Qu, D.; Xie, Z.; Tang, H.; Liu, J. *SmartMat* **2023**, *4*, e1200.

(19) Alt, C. D.; Müller, N. U.; Riegger, L. M.; Aktekin, B.; Minnmann, P.; Peppler, K.; Janek, J. *Joule* **2024**, *8*, 1–22.

(20) Liu, X.; Wu, X. Y.; Chang, B.; Wang, K. X. *Energy Storage Materials* **2020**, *30*, 146–169.

(21) Iosimovska, A. V.; Maltsev, A. P.; Chepkasov, I. V.; Oganov, A. R. *Applied Physics Letters* **2024**, *124*, 163904.